Journal of
Synchrotron Radiation

ISSN 0909-0495

Received 26 March 2007
Accepted 17 June 2007

Ray-trace calculations for *in situ* X-ray beam imaging

Nicholas R. Kyele and Roelof G. van Silfhout*

The University of Manchester, Manchester, UK. E-mail: r.vansilfhout@manchester.ac.uk

A two-dimensional beam-position and profile monitor for synchrotron X-ray beamlines was recently presented that was based on the principle of collection of scattered radiation from a thin polyimide foil. This paper presents a simple ray-trace model of the device, which can be used as a tool to calculate its response to changes in various device geometrical properties for a given beam size. The tool provides a quick way of predicting positional sensitivity, beam profile shape and intensity distribution. The theoretically obtained beam images are compared with data obtained from experiments carried out at the European Synchrotron Radiation Facility.

Keywords: X-rays; ray tracing; beam-position monitor; beam-profile monitor.

1. Introduction

Third-generation synchrotron radiation light sources provide very intense needle-like X-ray beams that are used on microscopic-sized samples. The samples to be studied are usually placed in a hutch that may be located at a distance of up to 70 m from the source. X-ray beam-position changes and/or deflections caused by either source movement or various other disturbances of the optical components of the beamline will cause significant deviations at the sample position and may result in the loss of focus at the sample or the beam missing the sample altogether. Beam-position monitors are therefore crucial to the successful operation of a beamline.

Various designs of beam-position monitors have been developed and implemented on synchrotron radiation beamlines. *In situ* beam-position monitors are the most effective; they monitor beam changes while the experiment is taking place and can therefore provide appropriate feedback to a control system for beam re-alignment. Most common methods for measuring beam position *in situ* include the collection of scattered photoelectrons from blade-based devices (Chen *et al.*, 1998), measure of change in photoconductivity of chemical-vapour-deposited diamond membranes (Bergonzo *et al.*, 1999; Schulze-Briese *et al.*, 2001), the use of modified ionization chambers (Menk *et al.*, 2007; Ilinski *et al.*, 2007; Siddons *et al.*, 2007) and direct exposure of the beam to silicon photodiodes (Southworth & Cowan, 1992; van Silfhout, 1998). Other devices are used to detect fluorescent radiation from metal foils (Alkire *et al.*, 2000) as well as scattered radiation from metal foils (van Silfhout, 1999).

Beam-position monitors that can also measure the profile of the beam have been developed. Revesz & White (2005) use a charge-coupled-device (CCD) imager device to generate two orthogonal intensity profiles of the beam. By passing the beam through a section of the beamline filled with helium at atmospheric pressure, they were able to capture the horizontal and vertical profiles of the luminescent light induced by the X-ray photons.

We have recently developed two-dimensional beam-position and profile monitors based on the collection of scattered radiation from a polyimide foil (Kyele *et al.*, 2005, 2007; van Silfhout *et al.*, 2007). By passing the X-ray beam through a foil placed in the path of the beam and collecting the scattered radiation at an angle of 90° using an active pixel sensor, we were able to track beam movements with a precision of at least 10 μm. A collimator placed between the scatter foil and the sensor adds the capability of X-ray beam imaging.

Here we present a software tool that provides a simple way to calculate the intensity distribution as measured at the sensor for various source sizes and shapes as an aid to interpreting and predicting measurements. This software-based model is used to study the effects of scatter foil parameters such as tilt angle and foil thickness; study the effect of collimator resolution on positional sensitivity and spatial resolution; predict the expected integrated intensity for a given collimator; study the effect of detected intensity on positional sensitivity; compare the ray-traced images with the data presented by recent studies.

The performance of the ray-trace calculations is investigated using simple scenarios that can be compared directly with theory. Although very advanced simulation tools exist [*e.g. GEANT4* (Agostinelli *et al.*, 2003), *SHADOW* (Lai & Cerrina, 1986)] for studying the interaction of X-rays with matter, they require very detailed geometry models that would make the process of optimizing the geometry very time consuming. Finally, ray-trace calculations are used to emulate and reproduce data from several experiments conducted at BM26A of the ESRF using active pixel (APS) and CCD detectors.

2. Ray-tracing model

The grey parallelogram in Fig. 1 represents the part of the scatter foil exposed to the X-ray beam. The foil has a thickness CF and is tilted under an angle α with respect to the incident beam. The detector is positioned below the scatter foil, perpendicular to the direction of travel of the beam at a distance L below the beam centre.

For a single simulation, 10^9 rays are generated from a set of 10^4 point sources that are located on that part of a plane through points A and C and parallel to the x direction that is exposed by the beam. For convenience, we shall refer to this area as the source plane from now on. The distribution of these point sources is generated in software such that they have a normal distribution around the beam centre and a spread equal to the projection of the beam size on the source plane. A Gaussian shape is generally accepted as the intensity distribution of a generic synchrotron radiation source. The spread of the beam on the source plane owing to the tilt and thickness of the foil is given by AC (see Fig. 1),

$$AC = \left[\left(\frac{CF}{\sin\alpha} + \frac{AE}{\tan\alpha}\right)^2 + (AE)^2\right]^{1/2}. \qquad (1)$$

Each point source generates 10^5 rays and for each ray a random direction of travel is generated defined by two angles, θ_x and θ_y. Here, both angles are defined to be zero for a ray travelling towards the sensor along its normal. X-rays scatter only very weakly, therefore the first Born or single-scattering approximation is used: all generated rays travel freely towards the detector without any absorption and/or further scattering. Neither do we consider inelastic scattering processes (Compton, fluorescence). We limit tracing rays which travel within a cone with angles of $\pm 35^\circ$ in order to limit computational overhead.

In our calculations we simulate two different experimental arrangements for *in situ* X-ray beam monitoring. The simplest case is the one in which the rays are allowed to travel freely towards the imager and their distribution over the sensor surface is recorded. Provided that the sensor is placed sufficiently close to the scatter foil, an appreciable intensity difference will be measured across the two-dimensional sensor. For a given ray, generated from a point source with a position (x_n, y_n) and a random direction of travel $(\theta_{xn}, \theta_{yn})$, the horizontal position of the ray on the sensor is given by

$$(x_{\rm pos}, y_{\rm pos}) = (x_n + L_n \tan\theta_{xn}, y_n + L_n \tan\theta_{yn}), \qquad (2)$$

where L_n is the distance from the point source to the detector as measured along the normal of the sensor. The horizontal position of the ray in (2) is calculated in spatial units of millimetres. If the position of the ray lies within the sensor's active area, it is recorded as a single count in the appropriate pixel, otherwise it is discarded.

In the second arrangement, we insert a collimator between the scatter foil and sensor. This arrangement will add beam imaging albeit at the expense of measured intensity levels. Only those rays that pass freely through a particular collimator hole and hit the sensor within its active area are counted. A ray that hits a wall (septum) of the collimator is discarded (see Fig. 2).

The use of a collimator enables the beam monitor to image the footprint of the beam on the scatter foil. We adapt a square-hole collimator design with a pitch p, hole size s and height D. We adapt the geometric efficiency E of a collimator as introduced by Anger (1964). This parameter is calculated as the part of the radiation from a point source, perpendicularly above and at a certain distance from a single collimator hole, that irradiates the open detector area of one pixel [normalized solid angle: $s^2/4\pi(L + D)^2$] multiplied by the average area in the source plane that is seen from any point on the detector pixel {region seen: $s^2[(L + D)/D]^2$} and normalized by the pixel area p^2,

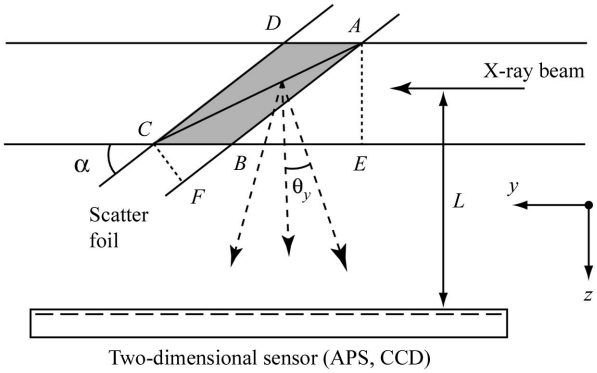

Figure 1
Side view of the scatter foil with a tilt angle α and thickness CF. The height of the beam is given by AE. X-rays are scattered from the part of the foil exposed by the beam (shaded region $ABCD$). Scattered X-rays are measured using a two-dimensional X-ray sensor. The x direction is pointing out of the plane of the paper.

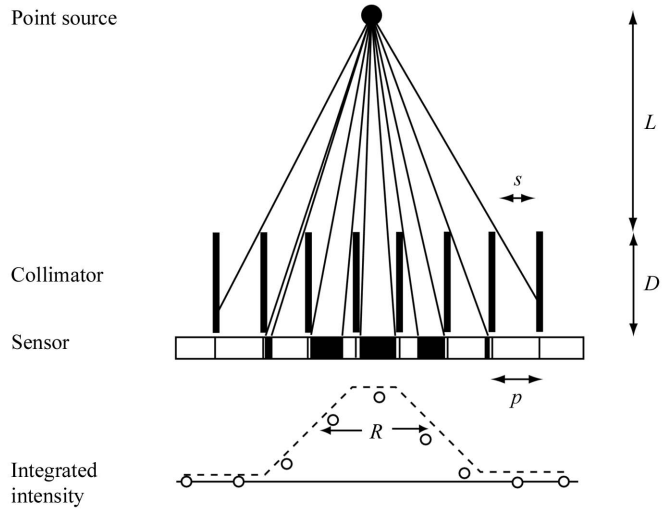

Figure 2
Schematic of a parallel-hole collimator (square hole size s, pitch p). Rays produced by a single point source illuminate only certain areas of the sensor (black). The resulting integrated intensity as measured with a pixellated detector is shown as open circles. The dashed line indicates the expected intensity distribution with a full width at half-maximum of R if the collimator is moved in the horizontal plane during the measurement.

$$E = \frac{s^2}{4\pi D^2}\frac{s^2}{p^2}. \quad (3)$$

The last term in (3) is equal to the effective *open area* for the square parallel-hole collimator case.

The full width at half-maximum (FWHM) of the intensity distribution owing to a point source is defined as the geometric resolution distance R and is given by

$$R = s\,[1 + (L/D)]. \quad (4)$$

This resolution distance, or spatial resolution, is, as expected, smallest for sources close to a very high collimator but never smaller than the hole size. The resolution for a square-hole collimator has an angular dependence and the above relation only holds in a direction parallel to the sides of the square hole. Owing to the tilt of the scatter foil, the spatial resolution also varies along the y direction.

3. Experimental and results

In an experiment carried out at bending-magnet beamline BM26A (DUBBLE) of the ESRF, a 127 µm-thick polyimide scatter foil (Kyele *et al.*, 2007) was used. The foil was positioned at an angle of 16° and the beam profile had a Gaussian shape with a reported FWHM of 1532 µm × 545 µm in the horizontal (x) and vertical (z) direction, respectively. The energy of the X-ray photons was fixed at 12 keV. We have used a similar size beam for a series of ray-trace calculations. The sensor used to record the scattered intensities was a monolithic active pixel sensor with a 3 mm-thick fibre-optic faceplate coated with a terbium-doped gadolinium oxysulfide (Gadox) phosphor. This sensor has an active area of 800 × 800 pixels with a single pixel area of 7 µm × 7 µm. Two experiments were performed: one without a collimator (Fig. 1) and one with a collimator (Fig. 2). The square-hole collimator used had a pitch p of 500 µm and a hole size s of 400 µm. Two collimator heights were used: for the active pixel sensor experiments D was 3 mm, whereas the measurement with the CCD detector was carried out with a collimator of height 50 mm.

3.1. Uncollimated detection

The intensity of the scattered radiation was recorded with the detector placed in close proximity to the scatter foil (see Fig. 1). The distance between the centre of the beam and the scintillator was 5 mm. The measured intensity distribution (Fig. 3*a*) is shown together with the result of our ray-trace calculation (Fig. 3*b*). In this calculation we used a slightly smaller size of the incident beam of 1432 µm × 545 µm. The ray-trace calculation is scaled to the data for comparison.

The difference image shown in Fig. 3(*c*) highlights the non-uniform response of the polycrystalline scintillator foil and systematic deviations around its perimeter as highlighted by the difference profiles shown in Fig. 3(*d*).

3.2. Collimated detection

A series of ray-trace calculations were performed to study the influence of key device parameters that include collimator height, open area and pitch on device response using a typical beam size. The collimator was placed at a distance L of 5 mm

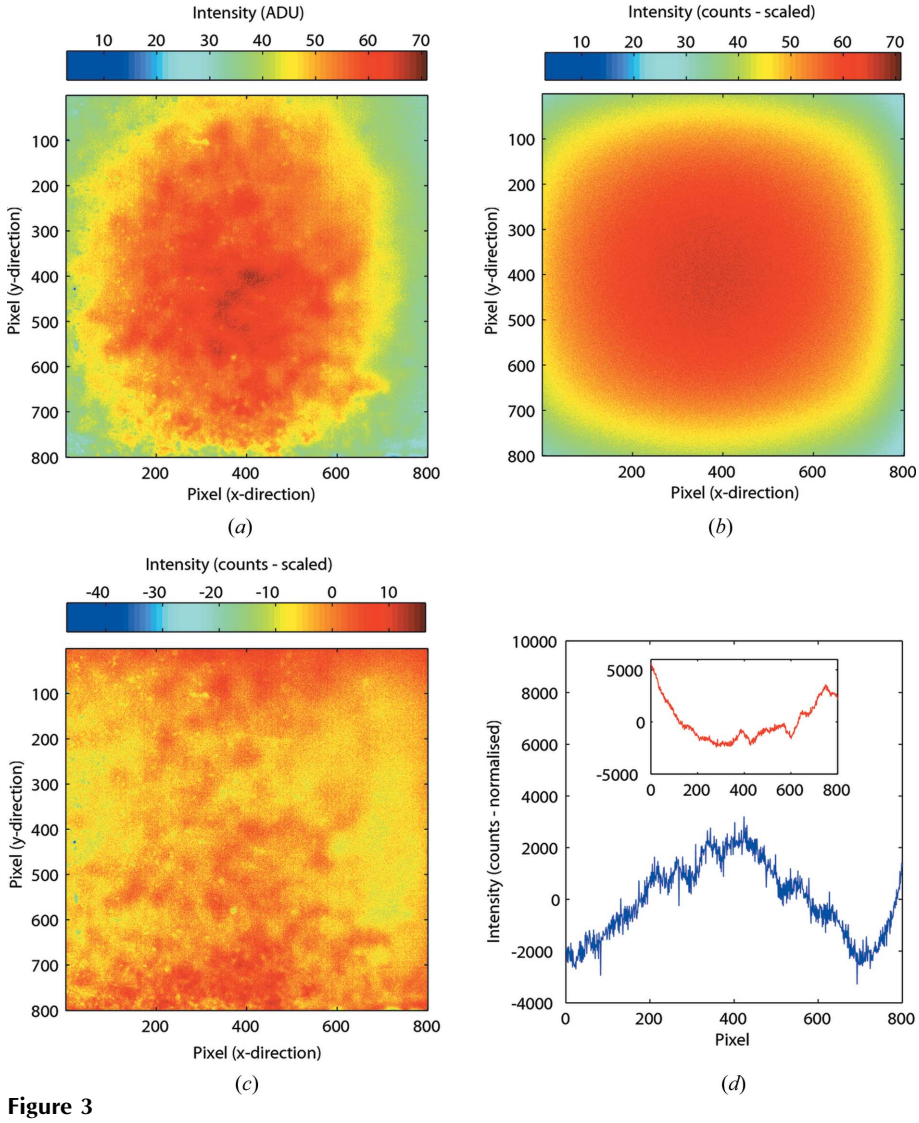

Figure 3
(*a*) False-colour image of the scattered intensity distribution by a polyimide foil as recorded by a sensor placed at a distance of 5 mm from the foil. (*b*) Ray-trace calculation. The ray-trace image has been scaled to (*a*). (*c*) The difference image obtained after subtracting the uncollimated ray-trace image from the uncollimated data image. (*d*) The horizontal and vertical (inset) profiles of the difference image are obtained by adding the columns and rows of (*c*), respectively.

below the scatter foil and the detector was located directly below the collimator. Most calculations were performed with an extended source similar in size to that of the X-ray beam used during experiments at BM26A with the active pixel detector. Finally, ray-trace calculations were compared with experimental data of two different experiments.

3.2.1. Collimator height. To determine the dependency of the integrated intensity on collimator height for our Gaussian source, ray-trace calculations were carried out with the collimator height increased in steps of 3 mm with a starting height of 3 mm. Fig. 4 shows the integrated intensity as a function of collimator height. Over this large range the spatial resolution distance R will vary from 1.1 to 2.6 times the collimator hole size s.

3.2.2. Collimator open area. A further parameter of interest is the effective open area of the collimator. Manufacturing restrictions of collimators place an upper limit on the effective open area of about 80%. For high-resolution collimators the effective open area would be no more than about 50%. In order to investigate the integrated intensity as a function of the open area for an extended source, we have performed a series of ray-trace calculations with a fixed collimator pitch, p, of 500 µm. For a point source the efficiency for a given collimator with an open area $(s/p)^2$ is given by (3).

The intensity of all the pixels in the image was summed to give the integrated intensity over the whole sensor area. Fig. 5 shows the change of the integrated intensity with reduction of collimator open area. The ray-trace results for a point source (circles) follow the expected behaviour (solid line). The result for the large beam size calculation gives, as expected, a curve that approximates the behaviour of a point source placed infinitely far from the collimator.

3.2.3. Collimator pitch. The pitch of a collimator is an important parameter that influences the width of the measured intensity distribution at the detector. For a point source, the FWHM of this distribution is given by the geometric resolution distance R. The intensity distribution as measured by the sensor is obtained by plotting the integrated intensity for each collimator hole. The horizontal and vertical profiles of the beam are then obtained by adding the rows and columns of the image, respectively. Fig. 6 illustrates the horizontal and vertical profiles of the ray-trace image. The FWHMs of the beam profiles are obtained by fitting a Gaussian to the data points.

Table 1
FWHM obtained for two different beam sizes using various collimator geometries.

The collimator thickness D is fixed at 3 mm. The standard deviation of each measurement is shown in parentheses. The scatter foil angle was kept at 16°.

			FWHM			
			Horizontal (µm)		Vertical (µm)	
Beam size (µm)	Collimator hole × septum (µm)	Collimator open area (%)	Ray-trace values	Analytical values	Ray-trace values	Analytical values
50 × 50	50 × 20	51.02	126 (2)	139	53 (3)	61
1532 × 545	100 × 100	25.00	1539 (24)	1553	551 (21)	549
	200 × 100	44.44	1586 (22)	1617	551 (16)	563
	300 × 100	56.25	1659 (14)	1719	564 (12)	585
	400 × 100	64.00	1770 (16)	1851	603 (13)	615

Various collimator geometries with the calculated horizontal and vertical beam FWHM values are shown in Table 1 together with theoretical values. The analytical values listed are calculated from a convolution of the resolution distance R for a given collimator geometry and the beam size used assuming that the resolution function has a Gaussian shape with a FWHM of R.

3.2.4. Positional sensitivity. To study the sensitivity of the device for beam movements, ray-trace calculations were carried out for collimators with different hole sizes and two different pitches. Beam position changes were generated with its centre of gravity shifted in the x and z directions.

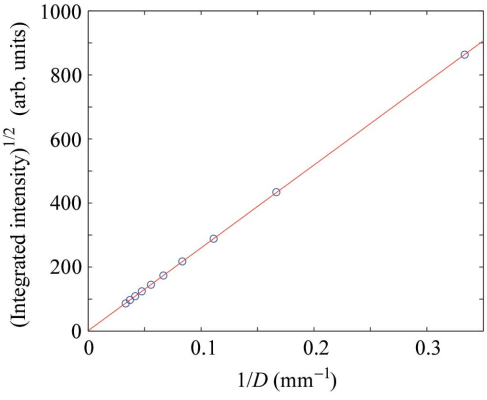

Figure 4
The intensity, as produced by a Gaussian beam, integrated over the whole detector as the collimator height is varied. The solid line represents the expected behaviour for a point source.

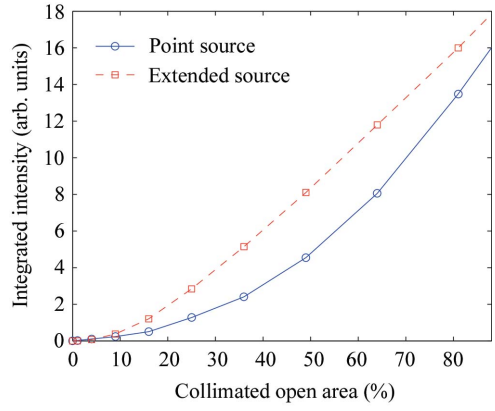

Figure 5
Graph of the integrated intensity over the whole sensor area calculated for a point source and an extended source taken with the collimated set-up. The solid line is a best-fit using (3) to the ray-trace result for a point source. The dashed line is a guide to the eye to the result of the calculations for an extended source with a FWHM of 4900 µm × 1200 µm.

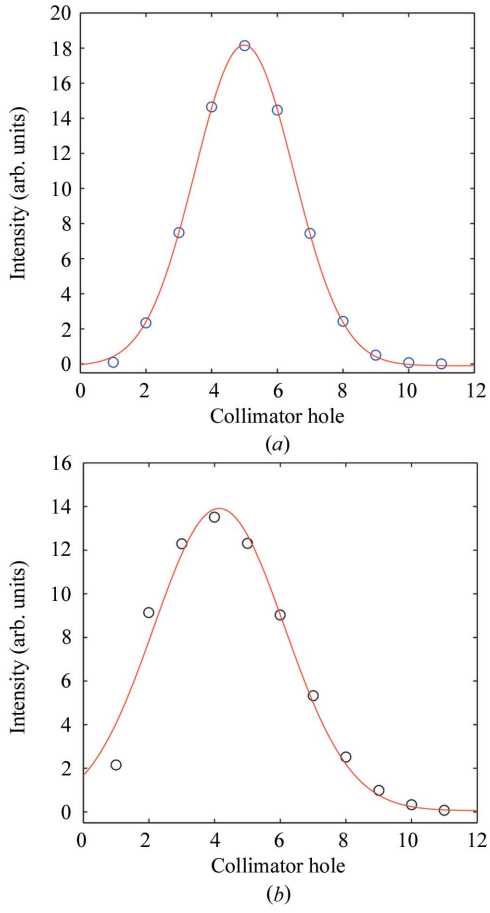

Figure 6
Horizontal (*a*) and vertical (*b*) beam profiles obtained from a ray-trace calculation. The solid lines represent the best-fit result of a Gaussian to the ray-trace calculations.

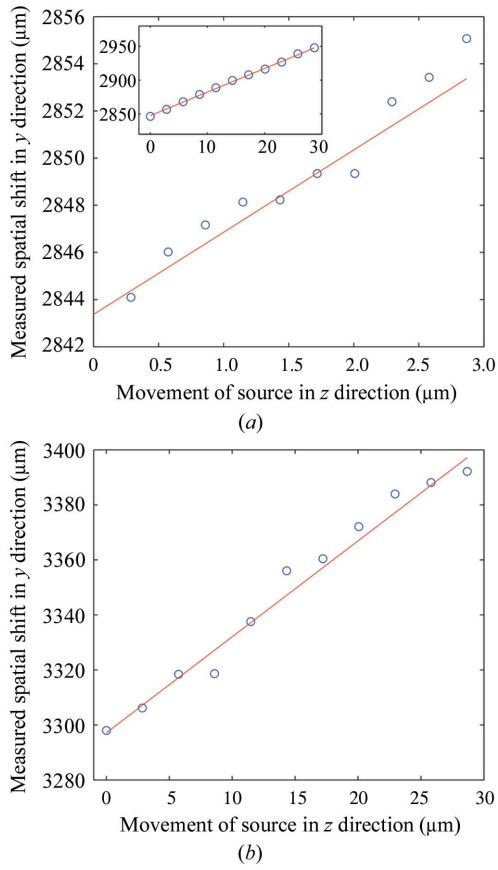

Figure 7
The measured movement of the centre of the beam profile for movement of the beam source in the *z* direction. (*a*) Calculated response for a device with 50 μm collimator and a beam with a FWHM of 50 μm × 50 μm. The inset shows the extended range which is to be compared with the calculations in (*b*) which are performed for our default collimator and a 1532 μm × 545 μm beam size. The solid line represents the expected response for a scatter foil angle of 16°.

For each step, a ray-trace calculation was carried out from which the horizontal and vertical beam profiles were obtained. Subsequently, Gaussians were fitted to the profiles in order to obtain their centre position that was used as an indicator of the beam position. Fig. 7 shows the measured movement of the beam plotted against the actual movement of the source for displacements in the *z* direction.

The spread shown in Fig. 7(*a*) for a 50 μm beam and matching collimator hole size predicts that the device will have a positional sensitivity of 0.3 μm. For a larger beam and collimator size, such as that present in our experiments at BM26A, the ray-trace calculations predict a positional sensitivity of 3 μm as inferred from Fig. 7(*b*).

3.2.5. Experiments. Experiments at BM26A (Kyele *et al.*, 2007) were conducted using a 3 mm-thick collimator with a default pitch of 0.5 mm and square hole size of 0.4 mm. One of the measured images is shown in Fig. 8(*a*). The result of our ray-trace calculation is shown in Fig. 8(*b*). A grid with the hole and septum dimensions of the collimator has been superimposed on the data images in Fig. 8 to highlight the asymmetry of the intensity distribution within a group of 7 μm × 7 μm sensor pixels located underneath particular collimator holes.

The peak intensity ratio between the non-collimated measurement and the collimated data presented in Fig. 8(*a*) of about 7:1 is reflected in the ratio of the peak intensities of the ray-traced calculations before scaling for both experiments.

Finally, we have also performed an experiment with a smaller beam size and a collimator of similar pitch and hole size as before but now with a much higher aspect ratio of 150:1 (Kyele *et al.*, 2005). The detector used was a CCD detector placed directly below the 50 mm-high collimator. Here, the beam did not show a Gaussian distribution because of a focusing mirror misalignment. The centre part of the beam has a reported FWHM of 889 μm and 484 μm in the horizontal and vertical direction, respectively. The foil tilt angle was 45°. An image of the footprint of the beam captured using the CCD detector is shown in Fig. 9(*a*). The square pixel size of the CCD imager was 45 μm. This large pixel size was due to 2 × 2 binning of individual pixel intensities.

From the experimental data it was clear that a pronounced tail in the *z* direction was present. For comparison, we have performed a ray-tracing calculation where the source was modelled by using two equally sized Gaussian sources with different intensities (intensity ratio 20:1) and shifted 1.6 mm

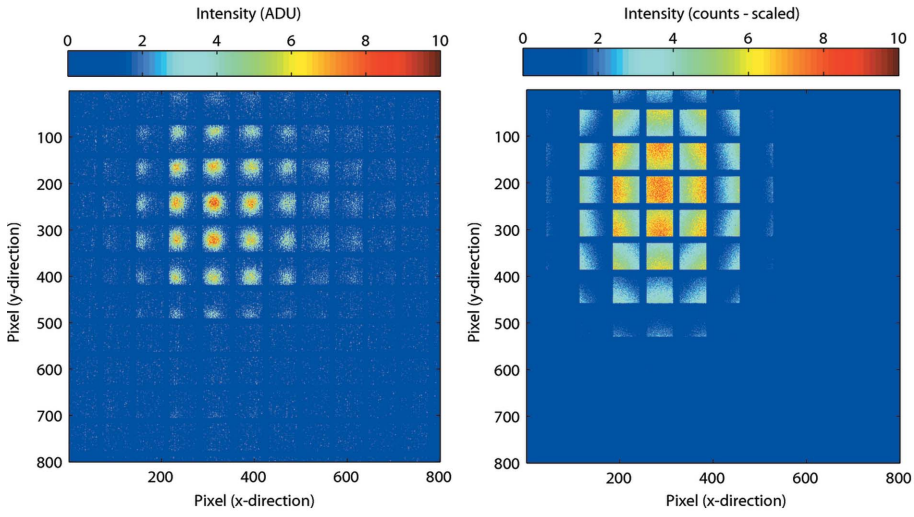

Figure 8
(*a*) Image of the footprint of the beam taken with the collimator. A grid with similar dimensions to the collimator has been superimposed onto the image for ease of comparison. (*b*) Ray-trace image obtained by recording rays that have successfully passed through a collimator with similar dimensions to the one used in (*a*). Note that the asymmetrical properties of the intensity distribution of the pixels under the collimator holes in the actual data image are reflected in the ray-trace image.

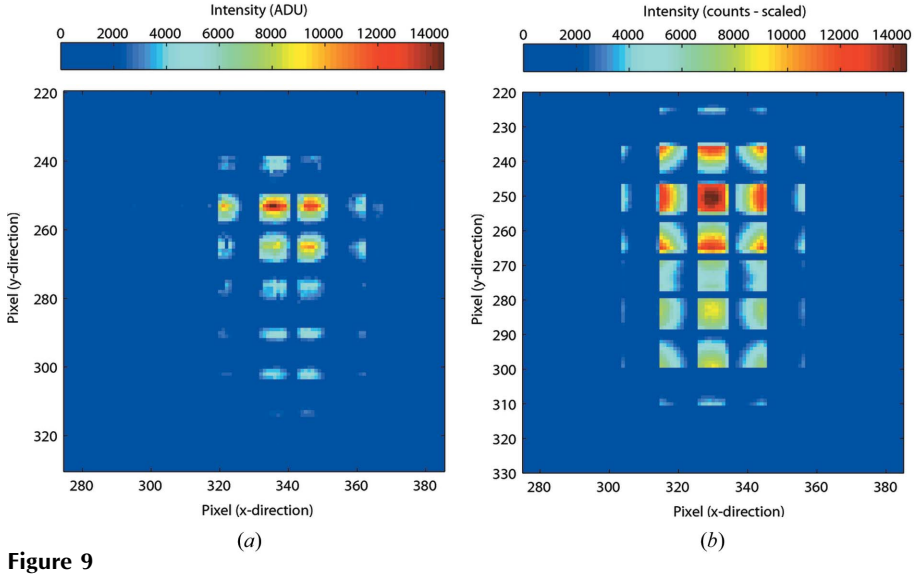

Figure 9
(*a*) Enlarged image of a smaller dimension beam taken with collimator for a foil tilt angle of 45°. A grid having similar dimensions to the collimator has been superimposed onto the image. (*b*) Ray-trace image obtained by recording rays that have successfully passed through a collimator with similar hole and septum dimensions to the one used in (*a*). Two beam spreads having a Gaussian distribution with their centres 1.6 mm apart were used as the source for the ray-trace image. The ray-trace image has been scaled to the data image.

vertically with respect to each other. The scaled ray-trace image is shown in Fig. 9(*b*).

4. Discussion

The presented ray-trace model has proven to be a valuable aid in interpreting the measurements that we obtained in our earlier studies. Moreover, this software has enabled us to investigate the behaviour and resolution of our beam monitor for new scattering geometries and different collimator designs. It is this capability that will allow us to further advance the technique and effectively predict device response to the change of various parameters. Our ray-trace calculations follow a rather basic approach. Several refinements could still be implemented. For example, currently we take a fixed number of rays in our calculations that does not relate to the actual number of rays scattered. The Monte Carlo procedure could be further refined to produce point sources distributed throughout the exposed volume of the scatter foil. Nevertheless, the simple model used provides results that compare well with our experiments.

The difference image obtained by subtracting the uncollimated ray-trace image from the data image reveals an uneven and random structure present in the data image. This effect is attributed to the rather course-grain material that makes up the scintillator foil used in the actual experiment. The use of crystalline scintillator materials (Bunk *et al.*, 2005) should solve this problem for high-resolution measurements. Near the edges of the sensor the calculated and measured patterns deviate significantly; this is probably related to issues with the simplification of the model and response of the scintillator. The horizontal and vertical profiles obtained from the uncollimated ray-trace image compare well with the polynomial-shaped profiles of the data image (Kyele *et al.*, 2007).

The collimated ray-trace images show that the intensity distribution of the pixels is concentrated near the edges of the collimator holes. This asymmetrical property of the intensity distribution is reflected in the measured image. Most of the rays generated at the centre of the footprint that impinge on the sensor having passed through a collimator hole will have travelled diagonally with respect to the normal of the sensor, and therefore are more likely to be recorded at the edges of the collimator holes that are adjacent to the centre of the imager. This effect is clearer for collimator holes that are further away from the pixel position below the centre of the footprint of the beam on the sensor. Although the intensity in the measured images shows this asymmetry, it is not right up to the positions of the septa. The explanation for this deviation is related to the construction of the collimators that were used.

They consist of many sheets with etched holes which are difficult to line up within a few micrometers. Also the individual etched foils show an incomplete etching of the corners which leave filleted corners. These issues will be resolved with the use of purpose-made capillary plates.

The results of beam-size measurements using various collimator geometries (see Table 1) show that there is a good agreement with that of a simple analytical model. The fact that the beam size derived from the ray-trace calculations is systematically lower than that calculated for the model is due to the fact that we have approximated the resolution function by a Gaussian.

Positional sensitivity of the collimated set-up as investigated by our ray-trace calculations is very good and compares well with the results of our earlier experiments. The use of smaller collimators with 50 μm holes is predicted to give submicrometer positional sensitivity, albeit at reduction in integrated intensity per hole of about 80 compared with that measured for 400 μm holes. Measuring with 300 ms integration time using our active pixel sensor detector will limit us to the use of collimators with a hole size of approximately 250 μm. However, for insertion-device beamlines with two to three orders of magnitude higher beam intensities, 50 μm collimators seem a good option. It must be pointed out that the positional sensitivity as derived from our simulations does not take into account the actual signal-to-noise ratio as measured by an actual detector.

In summary, we have successfully modelled a two-dimensional beam-position and profile monitor that measures the scattered radiation from a thin polyimide foil. The model uses the principle of ray tracing to obtain X-ray beam images for both collimated and uncollimated set-ups. The simulation has produced beam images and beam profiles that are in agreement with experimentally collected data. Furthermore, the model can be used as a tool to predict positional sensitivity, beam profiles and detected intensity for various beam, collimator and sensor parameters.

The authors would like to thank Dr W. Bras and the DUBBLE CRG staff for their support during experiments carried out at BM26A at the ESRF. This work is funded by EPSRC grant No. EP/E031994/1.

References

Agostinelli, S. *et al.* (2003). *Nucl. Instrum. Methods*, A**506**, 250–303.
Alkire, R. W., Rosenbaum, G. & Evans, G. (2000). *J. Synchrotron Rad.* **7**, 61–68.
Anger, H. O. (1964). *J. Nucl. Med.* **5**, 515–531.
Bergonzo, P., Brambilla, A., Tromson, D., Marshall, R. D., Jany, C., Foulon, F., Gauthier, C., Solé, V. A., Rogalev, A. & Goulon, J. (1999). *J. Synchrotron Rad.* **6**, 1–5.
Bunk, O., Pfeiffer, F., Stampanoni, M., Patterson, B. D., Schulze-Briese, C. & David, C. (2005). *J. Synchrotron Rad.* **12**, 795–799.
Chen, J.-R., Ueng, T. S., Hsiung, G. Y., Lin, T. F., Lee, C. T., Tsai, S. L. & Chang, S.-L. (1998). *J. Synchrotron Rad.* **5**, 621–623.
Ilinski, P., Hahn, U., Schulte-Schrepping, H. & Degenhardt, M. (2007). *AIP Conference Proceedings 879*, edited by J.-Y. Choi and C. Rah, pp. 782–785. Melville, NY: American Institute of Physics.
Kyele, N. R., Decanniere, K. & van Silfhout, R. G. (2005). *J. Synchrotron Rad.* **12**, 800–806.
Kyele, N. R., Manolopoulos, S., Nikitenko, S. & van Silfhout, R. G. (2007). *J. Appl. Phys.* **101**, 064901.
Lai, B. & Cerrina, F. (1986). *Nucl. Instrum. Methods*, A**246**, 337–341.
Menk, R. H., Giuressi, D., Arfelli, F. & Rigon, L. (2007). *AIP Conference Proceedings 879*, edited by J.-Y. Choi and C. Rah, pp. 1109–1112. Melville, NY: American Institute of Physics.
Revesz, P. & White, J. A. (2005). *Nucl. Instrum. Methods*, A**540**, 470–479.
Schulze-Briese, C., Ketterer, B., Pradervand, C., Brönnimann, C., David, C., Horisberger, R., Puig-Molina, A. & Graafsma, H. (2001). *Nucl. Instrum. Methods*, A**467–468**, 230–234.
Siddons, D. P., Kuczewski, A. J., Yu, B., Warren, J., Rudati, J., Fuoss, P., Hastings, J. B., Kaspar, J. D., Meyer, D. A. & Collaboration, S. (2007). *AIP Conference Proceedings 879*, edited by J.-Y. Choi and C. Rah, pp. 1176–1179. Melville, NY: American Institute of Physics.
Southworth, S. H. & Cowan, P. L. (1992). *Nucl. Instrum. Methods*, A**319**, 51–55.
Silfhout, R. G. van (1998). *Nucl. Instrum. Methods*, A**403**, 153–160.
Silfhout, R. G. van (1999). *J. Synchrotron Rad.* **6**, 1071–1075.
Silfhout, R. G. van, Manolopoulos, S., Kyele, N. R. & Decanniere, K. (2007). *Sens. Actuators A Phys.* **133**, 82–87.